Supplementary Information (SI)

Structure-performance correlation on bimetallic catalysts for selective CO_2 hydrogenation

Sibei Zou [a*], Lizhuo Wang [b], Hao Wang [a], Xingmo Zhang [b], Haoyue Sun [b], Xiaozhou Liao [a], Jun Huang [b*], and Assaad R. Masri [a]

[a] School of Aerospace, Mechanical and Mechatronic Engineering, The University of Sydney, New South Wales 2006, Australia

[b] School of Chemical and Biomolecular Engineering, The University of Sydney, New South Wales 2006, Australia

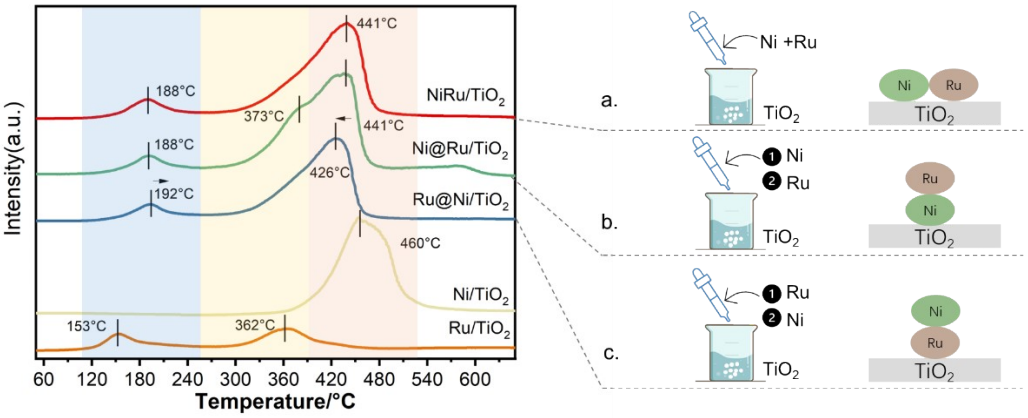

Figure S1. H_2-TPR experiment over all samples with different impregnation sequences and the relative experiment schematic: (a) NiRu/TiO_2, (b) Ni@Ru/TiO_2, (c) Ru@Ni/TiO_2.

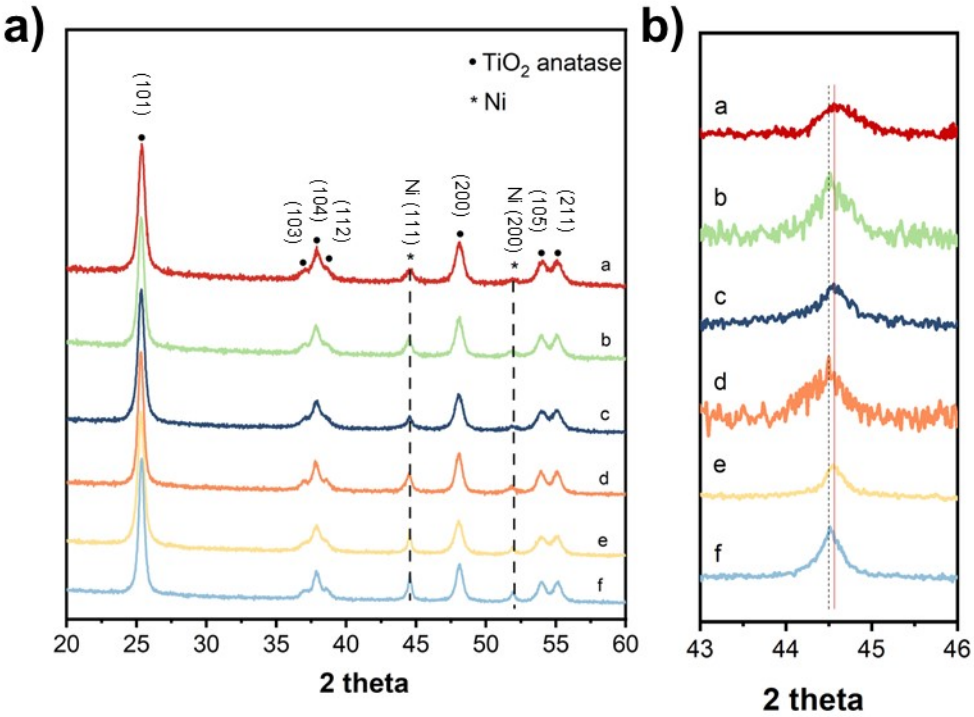

Figure S2. (a) XRD results of all catalysts (a. NiRu/TiO_2-300, b. NiRu/TiO_2-500, c. Ni@Ru/TiO_2-300, d. Ni@Ru/TiO_2-500, e. Ru@Ni/TiO_2-300, f. Ru@Ni/TiO_2-500); (b) magnified region of XRD Ni(111) peak shift

The Ni (111) peaks shift slightly to a lower diffraction angle, possibly due to the formation of a Ni-Ru solid solution formation. Even though they all show the tendency to shifting to lower diffraction angle in samples reduced at 500 °C, these shifts are very small. This is because of the relatively low molar ratio of Ru and Ni (1: 17.2) and the small Ni nanoparticle size at around 1.1 nm. At this stage, there should be slight lattice distortion due to such small amount of Ru dispersed into Ni nanoparticles as alloy formation, which will have very small affection on lattice distance. Therefore, further characterizations such as STEM-HAADF, EDS, EELS, and XPS are necessary to reveal the bimetallic structures.

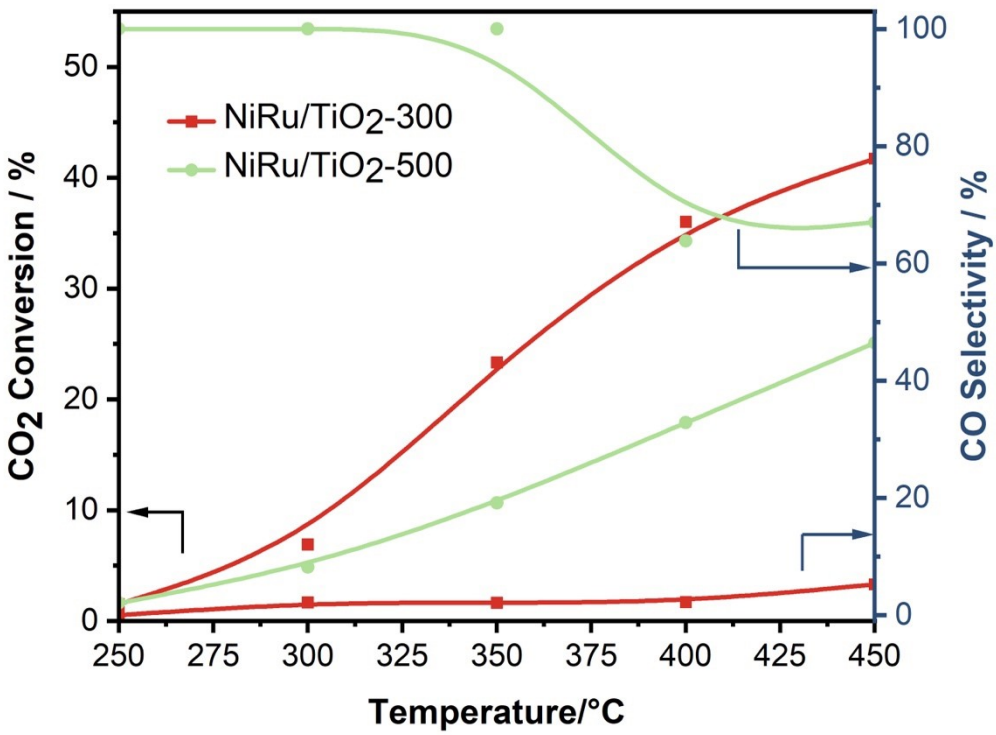

Figure. S3 CO_2 conversion and product selectivity of NiRu/TiO_2-300 and NiRu/TiO_2-500 catalysts. The reactant gas mixture (15% CO_2 : 60% H_2 : 25% N_2) was fed into the reactor at a constant WHSV (Weigh Hourly Space Velocity) of 37800 mL•g^{-1}•h^{-1}.

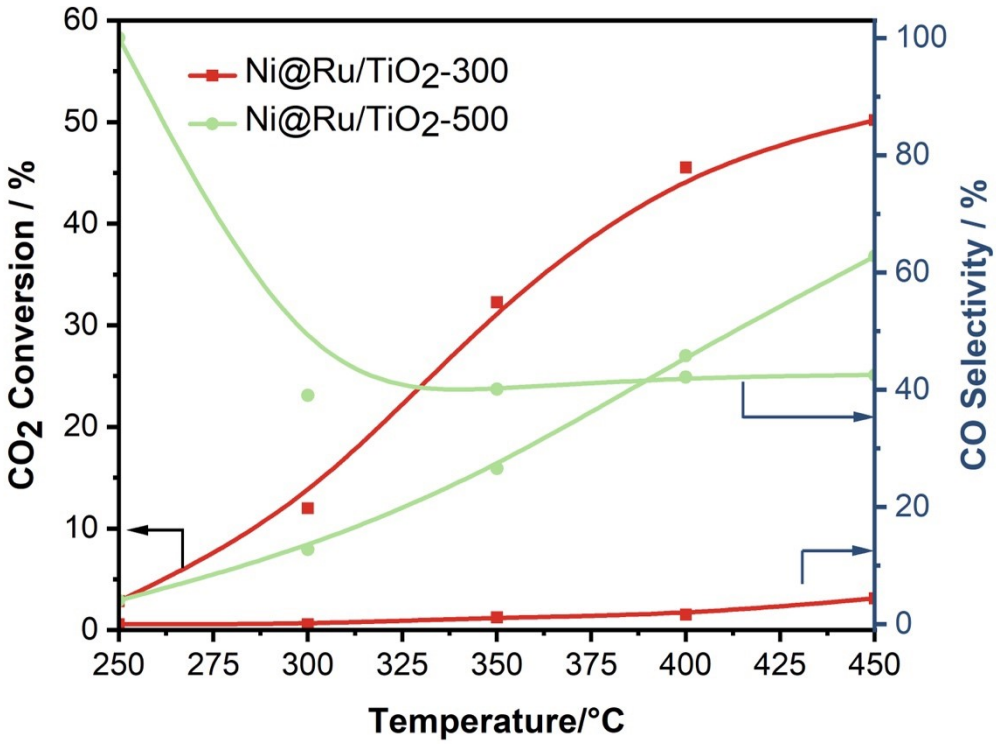

Figure. S4 CO_2 conversion and product selectivity of Ni@Ru/TiO_2-300 and Ni@Ru/TiO_2-500 catalysts. The reactant gas mixture (15% CO_2 : 60% H_2 : 25% N_2) was fed into the reactor at a constant WHSV (Weigh Hourly Space Velocity) of 37800 mL•g^{-1}•h^{-1}.

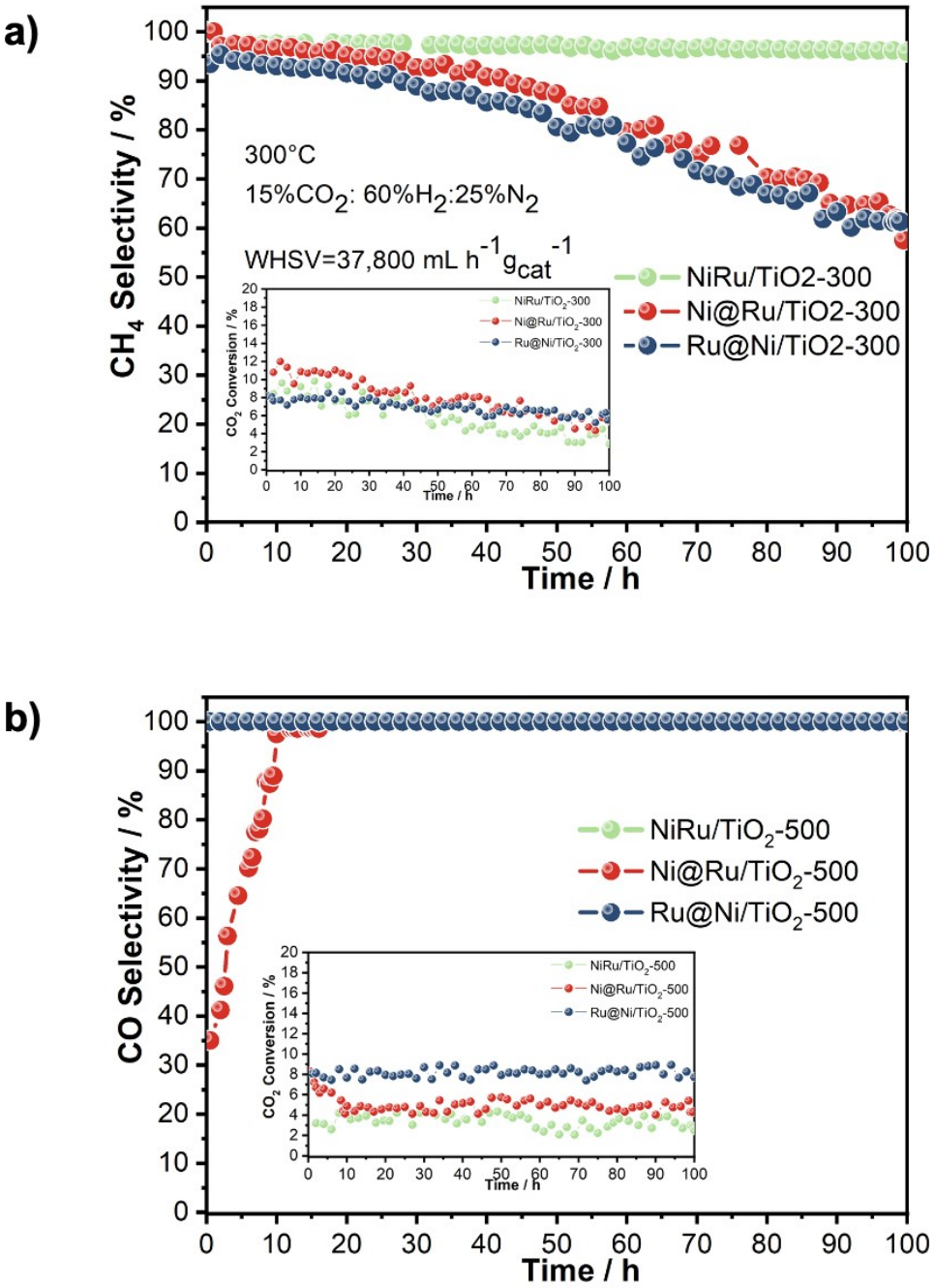

Figure. S5 (a) CH_4 selectivity and CO_2 conversion (left-bottom corner image) 100-h stability tests over catalysts reduction at 300 °C; (b) CO selectivity and CO_2 conversion (left-bottom corner image) 100-h stability tests over catalysts reduction at 500 °C.

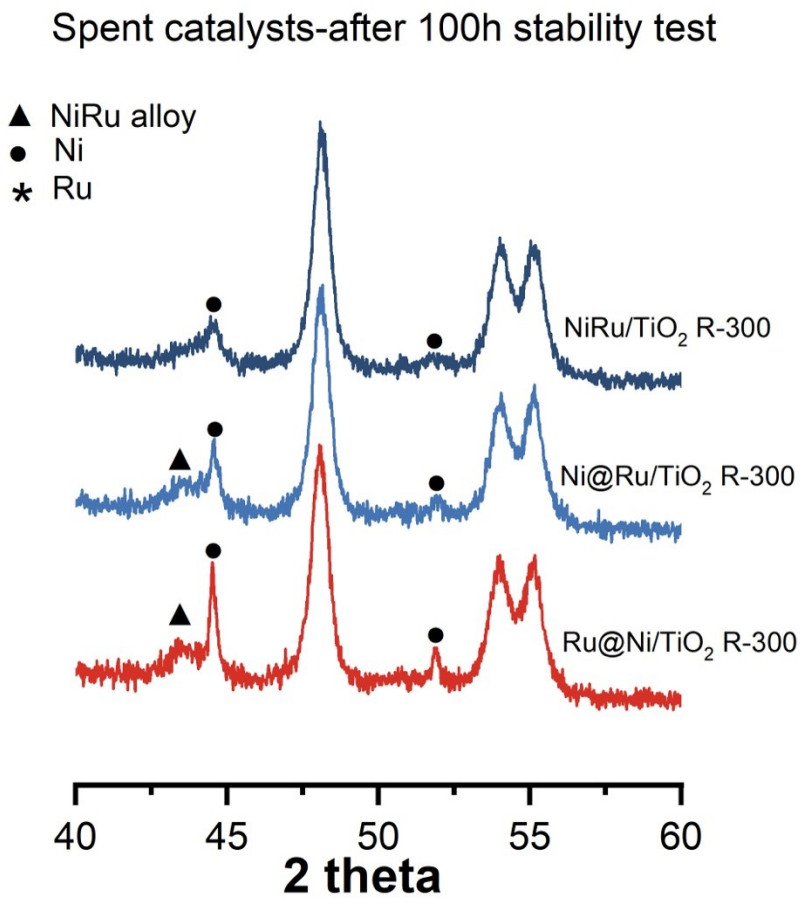

Figure. S6 The XRD results of catalysts (NiRu/TiO_2-300, Ni@Ru/TiO_2-300, and Ru@Ni/TiO_2-300) after 100-h long-term stability tests.

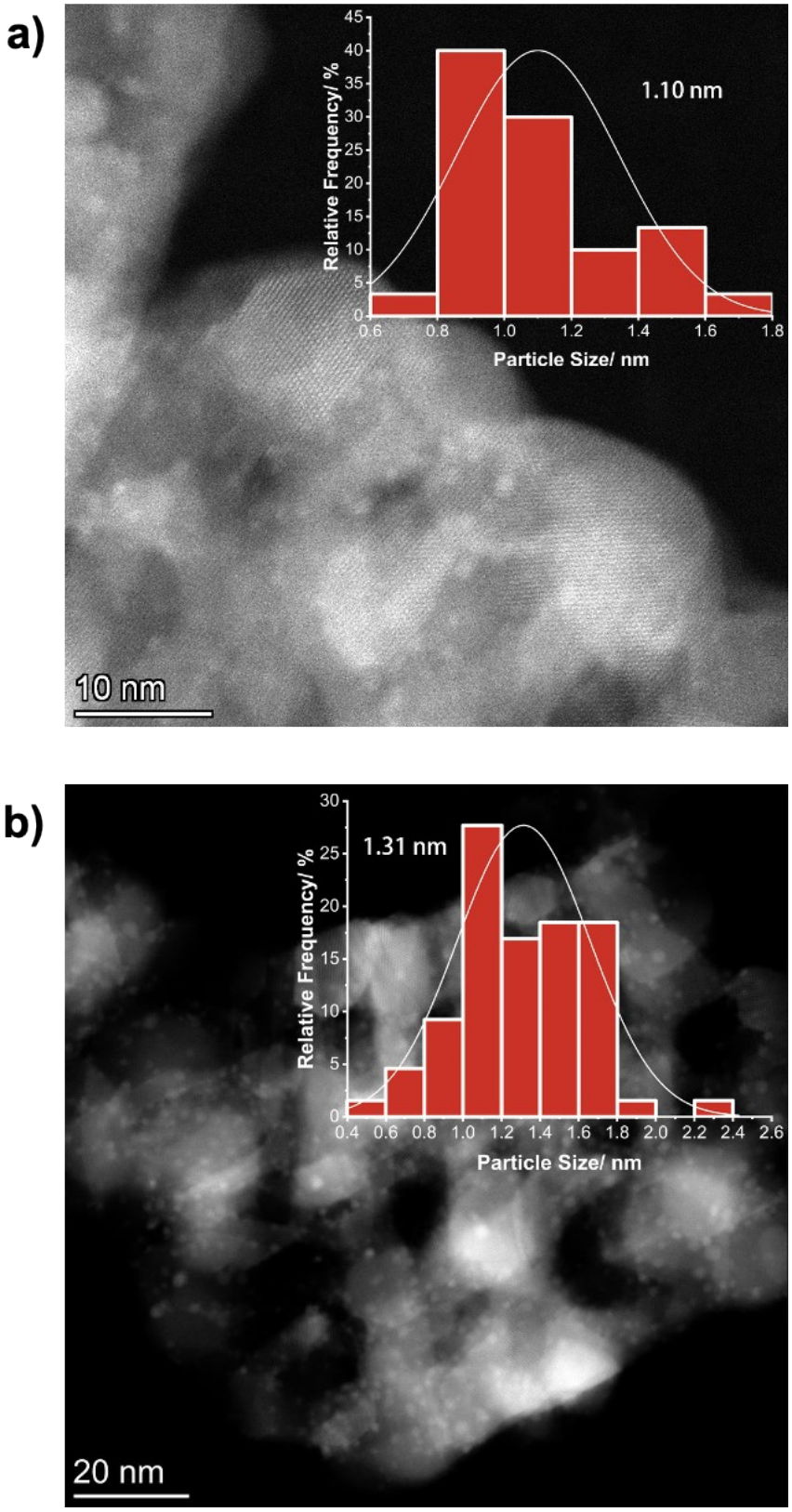

Figure. S7 STEM-HAADF: nanoparticle sizes of (a) NiRu/TiO_2-300; (b) NiRu/TiO_2-500.

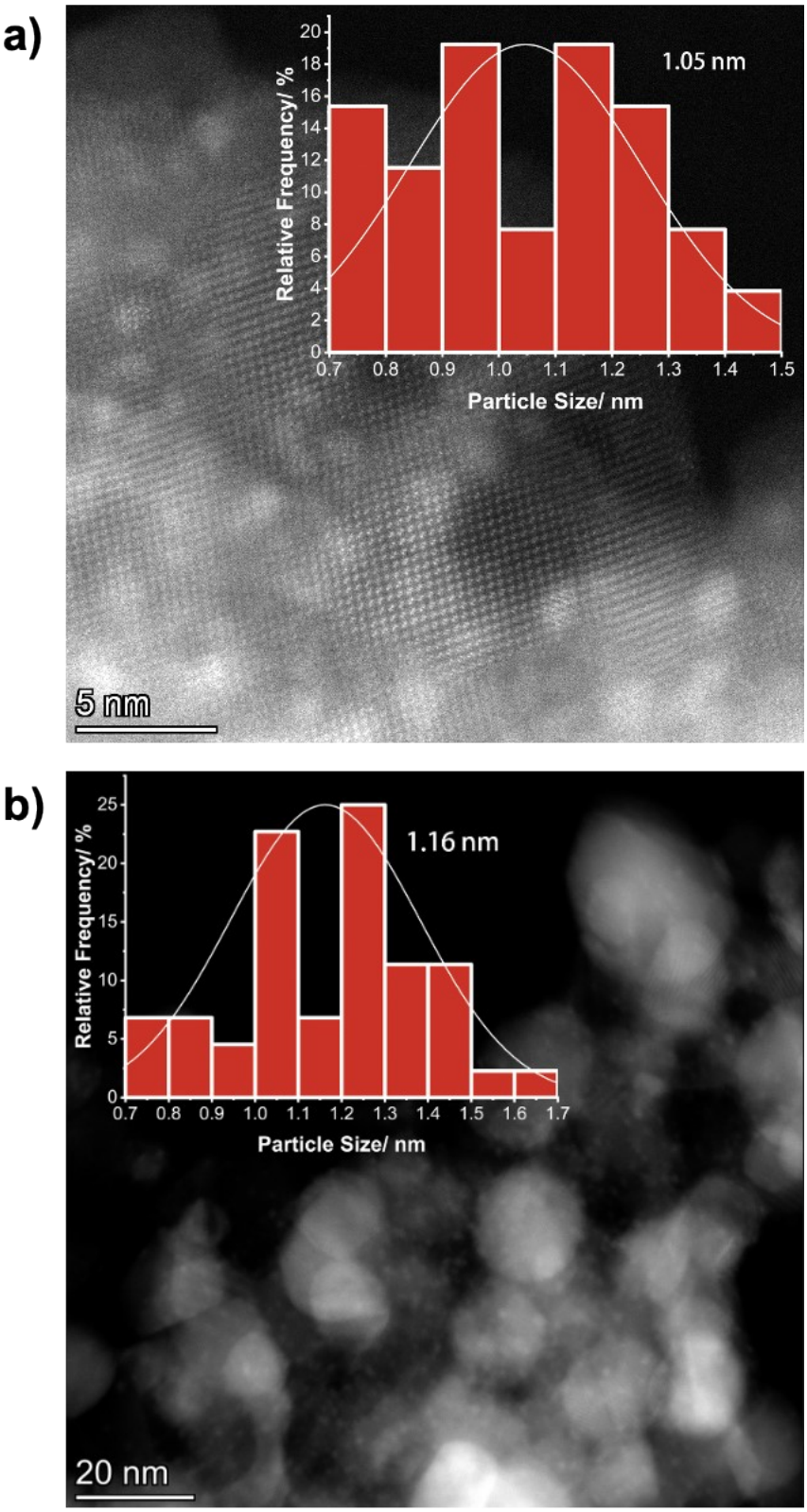

Figure. S8 STEM-HAADF: nanoparticle sizes of (a) Ni@Ru/TiO_2-300; (b) Ni@Ru/TiO_2-500.

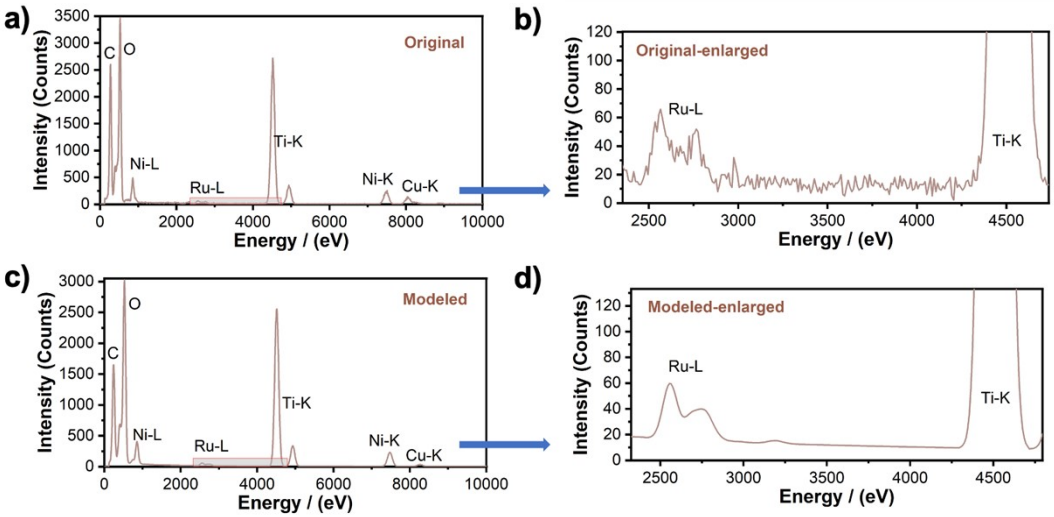

Figure S9. (a) The original and the enlarged Ru area spectra of the EDS in Fig. 2f; (b) the corresponding empirical modelled and the enlarged Ru area spectra of the EDS based on the Ni metal density Fig.2f.

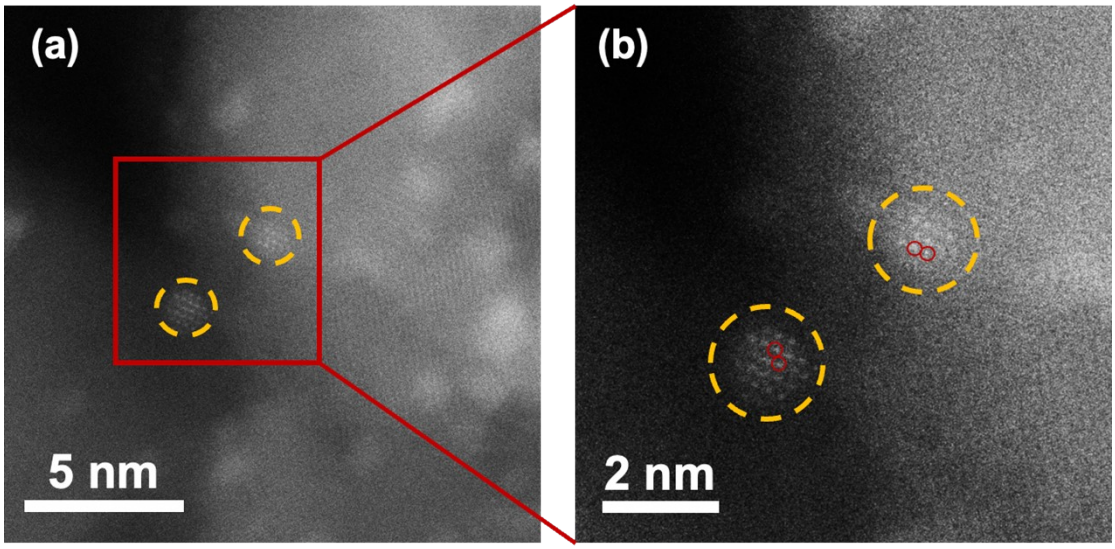

Figure. S10 (a) STEM-HAADF of NiRu alloy clusters highlighted in yellow circles and (b) the magnification STEM-HAADF region of the NiRu alloy clusters with distinguish Ru atoms in red circles.

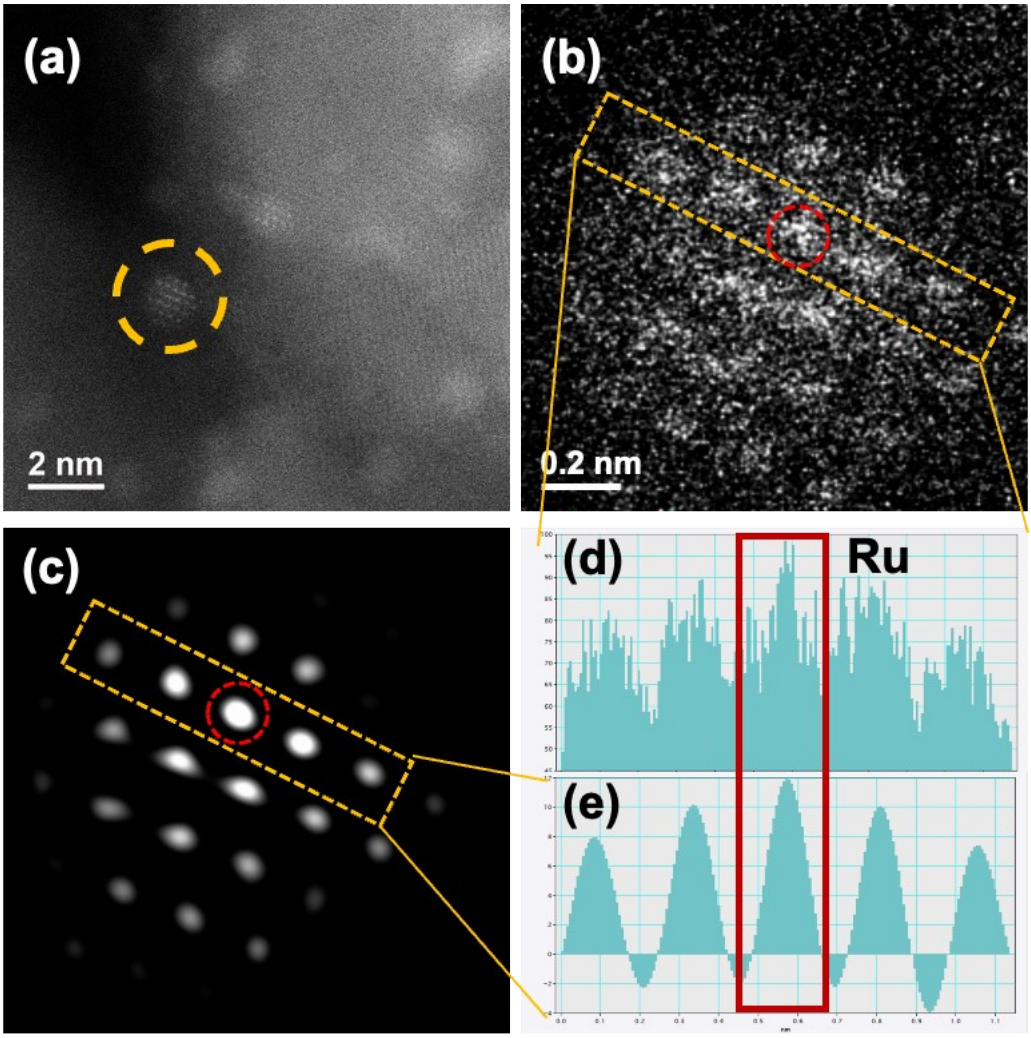

Figure. S11 (a) STEM-HAADF of Ru@Ni/TiO_2-500 and (b) the corresponding enlarge image of yellow circle in (a): Ru single atoms in small Ni nano-clusters in red circle. (c) The filtered inverse Fast Fourier Transform (IFFT) image of (b). (d) The line intensity profile of a row of atoms in the yellow region of (b). (e) The corresponding line intensity profile of a row of atoms in the yellow region of (c).

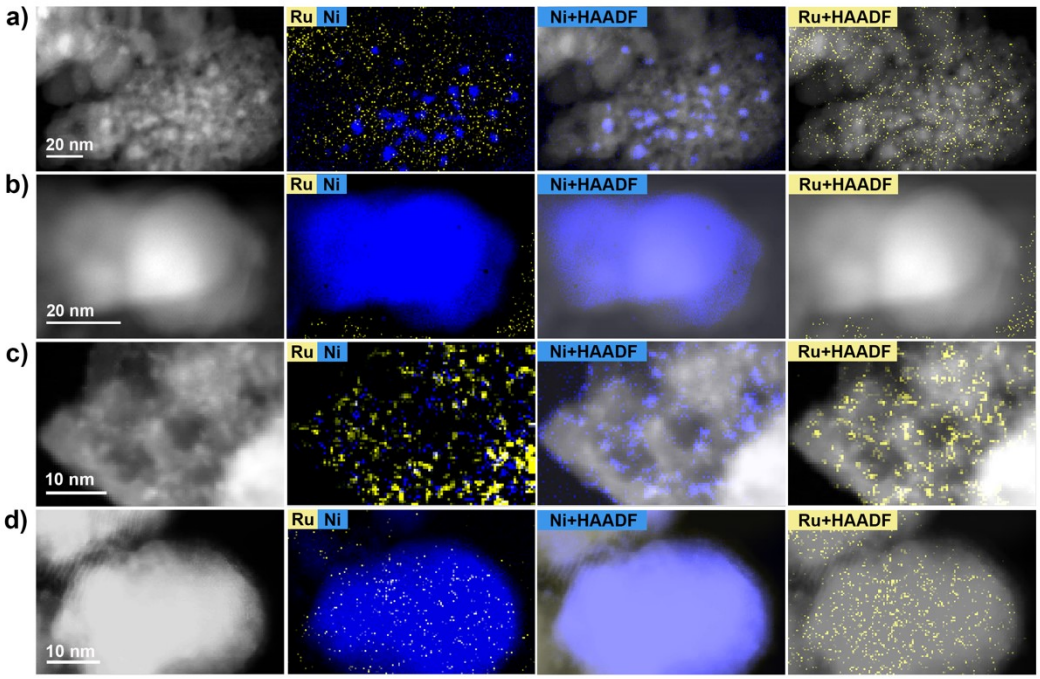

Figure S12. (a) STEM-HAADF of small nanoclusters in Ru@Ni/TiO_2-300 and the corresponding Ni and Ru EELS mappings; (b) STEM-HAADF of large nanoclusters in Ru@Ni/TiO_2-300 and the corresponding Ni and Ru EELS mappings; (c) STEM-HAADF of small nanoclusters in Ru@Ni/TiO_2-500 and the corresponding Ni and Ru EELS mappings; (d) STEM-HAADF of large nanoclusters in Ru@Ni/TiO_2-500 and the corresponding Ni and Ru EELS mappings.

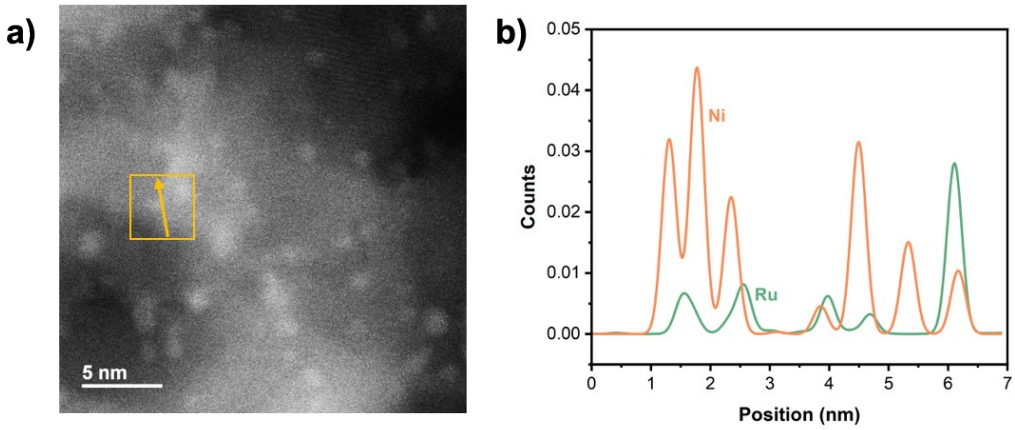

Figure. S13 (a) STEM-HADDFof Ru@Ni/TiO_2-500; (b) the corresponding EDS line scanning in the area of the yellow box in the direction of the yellow arrow.

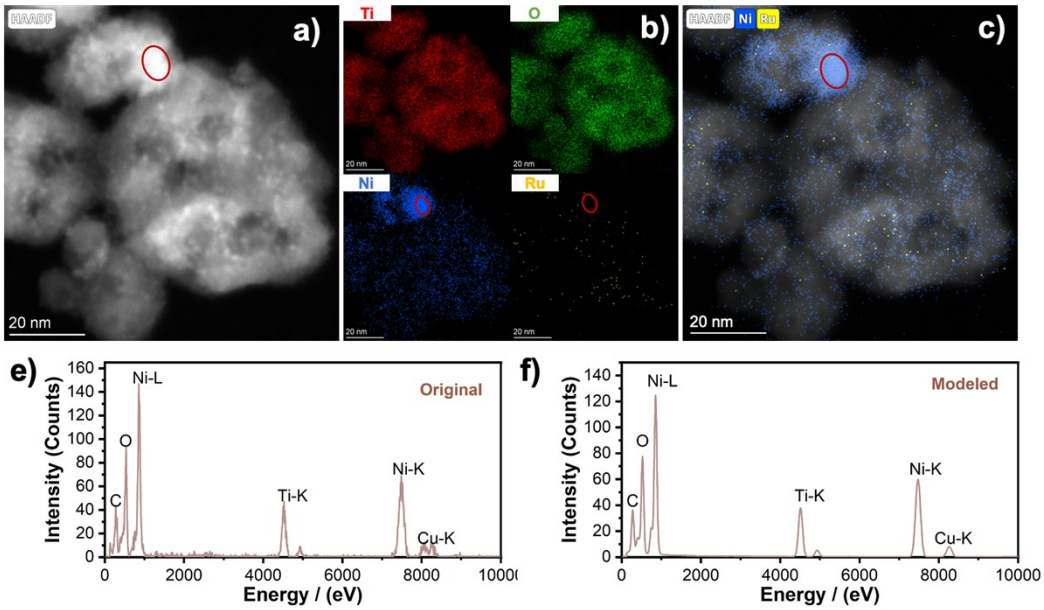

Figure. S14 (a) STEM-HAADF of NiRu/TiO_2-300; (b) the corresponding EDS mapping; (c) a combined Ni and Ru EDS mapping; (e) the original spectrum of the EDS in the nanoparticle highlighted in a red circle; (f) the corresponding empirical modelled spectrum of the EDS based on the Ni metal density in the nanoparticle highlighted in a red circle.

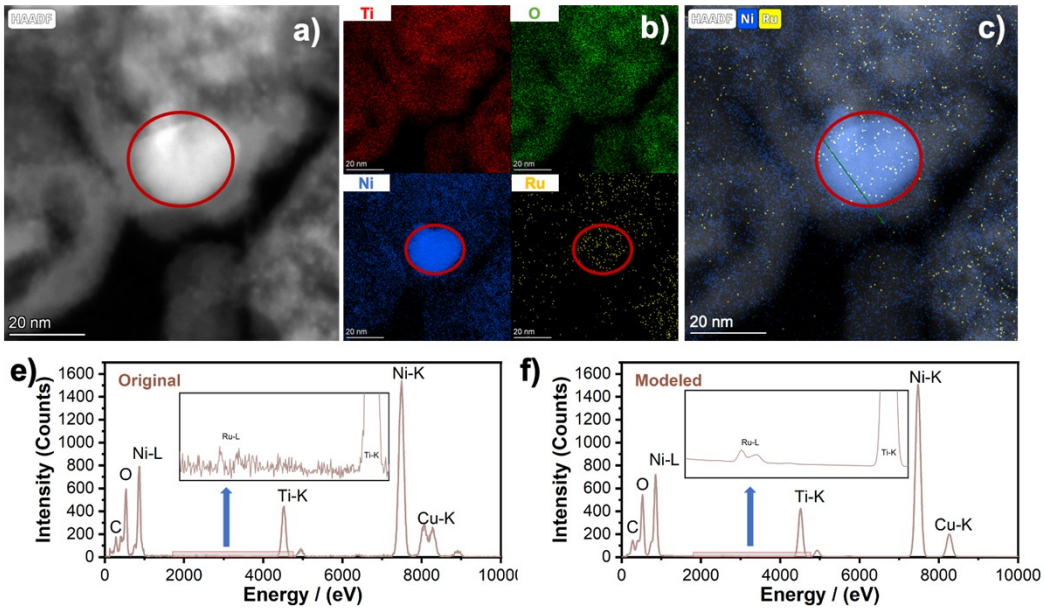

Figure. S15 (a) STEM-HAADF of NiRu/TiO_2-500; (b) the corresponding EDS mapping; (c) a combined Ni and Ru EDS mapping; (e) the original spectrum of the EDS in the nanoparticle highlighted in a red circle and the corresponding enlarged area of Ru-L; (f) the corresponding empirical modelled spectrum of the EDS based on the Ni metal density in the nanoparticle highlighted in a red circle and the enlarged area of Ru-L.

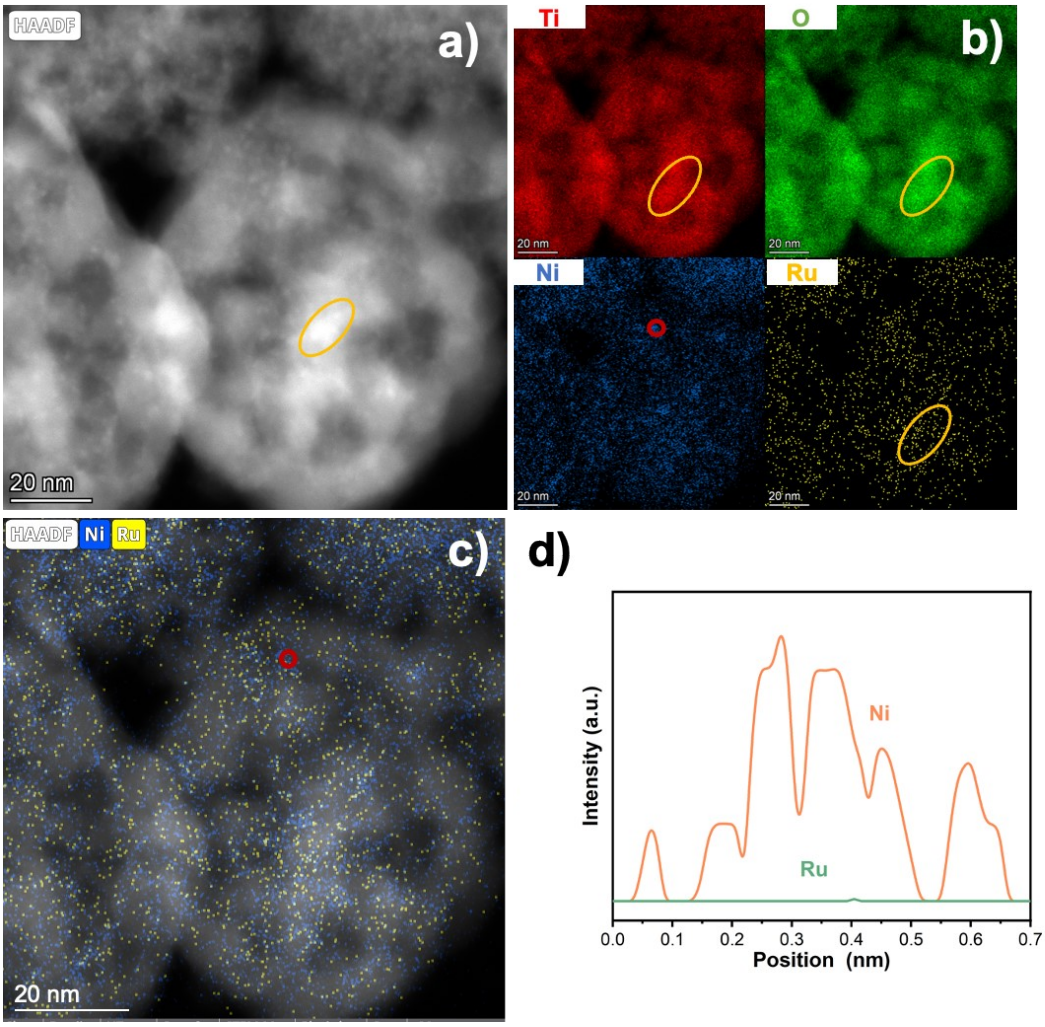

Figure. S16 (a) STEM-HAADF of Ni@Ru/TiO_2-300; (b) the corresponding EDS mapping; (c) a combined Ni and Ru EDS mapping; (d) the EDS line scaning of Ni and Ru element distribution in the small nanoparticle highlighted in the red circle.

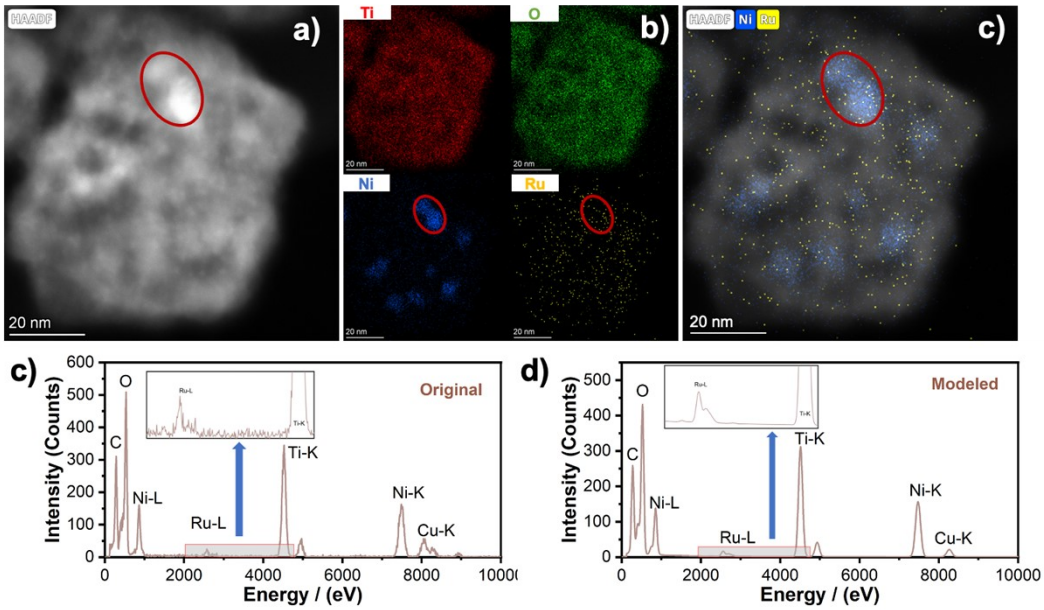

Figure. S17 (a) STEM-HAADF of Ni@Ru/TiO_2-500; (b) the corresponding EDS mapping; (c) a combined Ni and Ru EDS mapping; (e) the original spectrum of the EDS in the nanoparticle highlighted in a red circle and the corresponding enlarged area of Ru-L; (f) the corresponding empirical modelled spectrum of the EDS based on the Ni metal density in the nanoparticle highlighted in a red circle and the enlarged area of Ru-L.

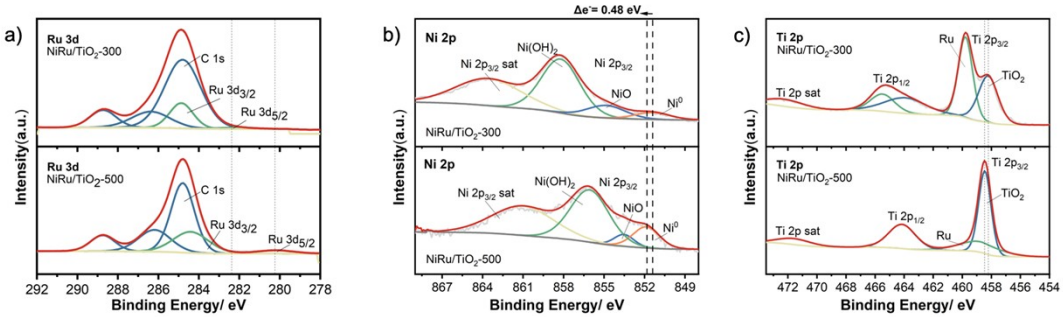

Figure. S18 (a) the C 1s and Ru 3d XPS results of NiRu/TiO_2-300 and NiRu/TiO_2-500; (b) the Ni 2p XPS results of NiRu/TiO_2-300 and NiRu/TiO_2-500; (c) the Ti 2p XPS results of NiRu/TiO_2-300 and NiRu/TiO_2-500.

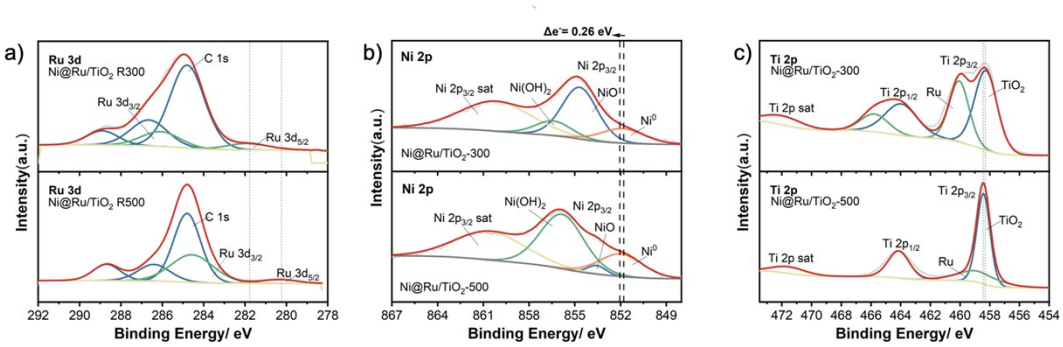

Figure. S19 (a) the C 1s and Ru 3d XPS results of Ni@Ru/TiO_2-300 and Ni@Ru/TiO_2-500; (b) the Ni 2p XPS results of Ni@Ru/TiO_2-300 and Ni@Ru/TiO_2-500; (c) the Ti 2p XPS results of Ni@Ru/TiO_2-300 and Ni@Ru/TiO_2-500.

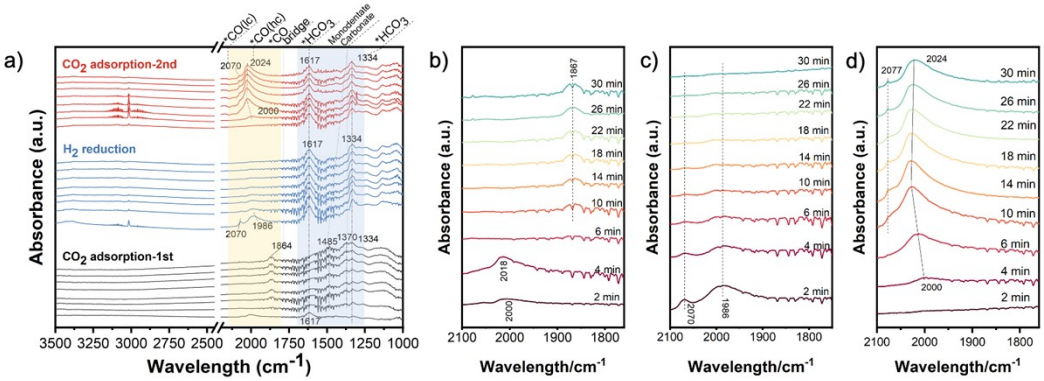

Figure. S20 The transition-state in-situ DRIFTS of Ru@Ni/TiO_2-300 and the corresponding magnify area of *CO in the procedure of: (b) CO_2 adsorption-1st; (c) H_2 reduction; (d) CO_2 adsorption-2nd.

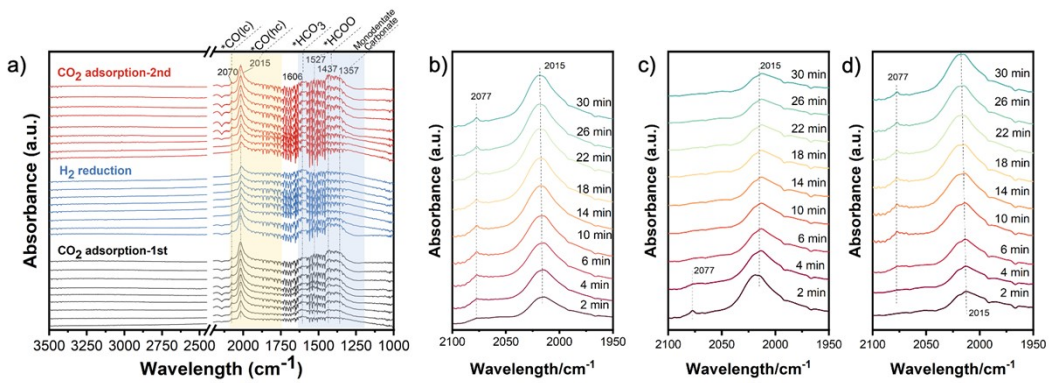

Figure. S21 The transition-state in-situ DRIFTS of Ru@Ni/TiO_2-500 and the corresponding magnify area of *CO in the procedure of: (b) CO_2 adsorption-1st; (c) H_2 reduction; (d) CO_2 adsorption-2nd.

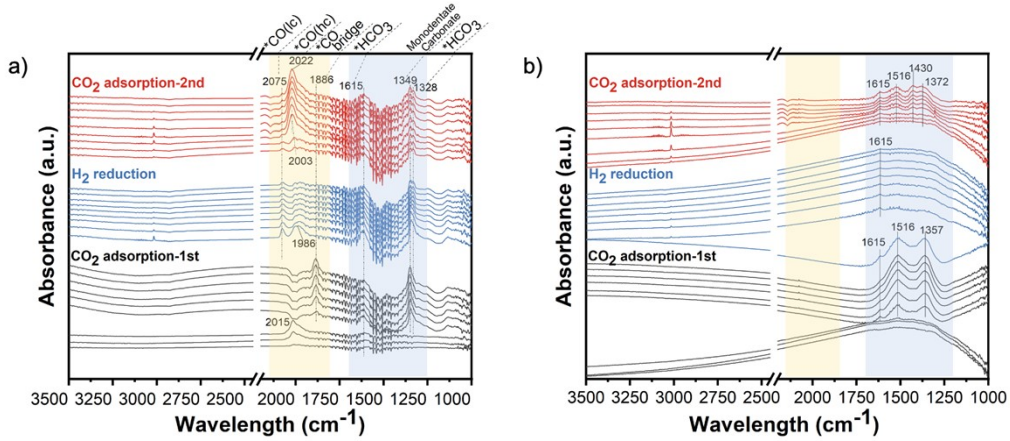

Figure. S22 The transition-state in-situ DRIFTS of (a) Ru/TiO_2 and (b) Ni/TiO_2. Transition-state in-situ DRIFTS experiments are conducted by alternatively switching the adsorption gas three times to first 5% CO_2 in N_2, then 20% H_2 in N_2, and finally 5% CO_2 in N_2 again under the temperature at 300 °C

As reference, the transition-state experiments are also conducted on Ru/TiO_2 and Ni/TiO_2 (Fig. S22). It is revealed that only Ru atoms can directly dissociate CO_2 to *CO species even without hydrogen. But both Ru and Ni atoms can dissociate H_2. And the H_2 spillover phenomenon can be observed on Ni/TiO_2.

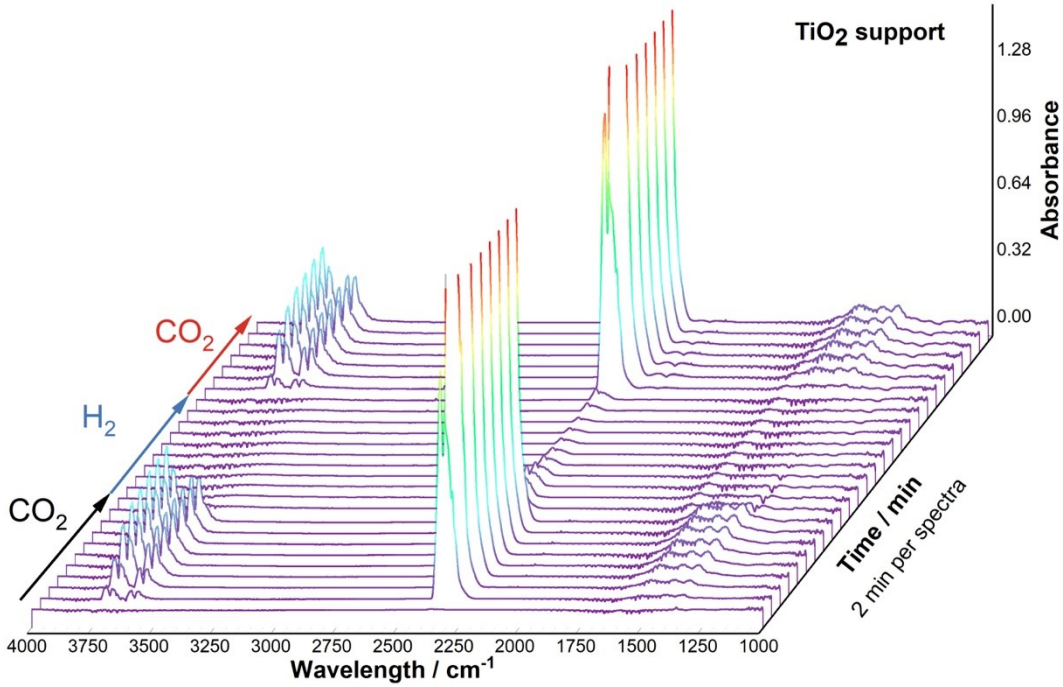

Figure. S23 3D graphs of the absorption intensity in transition-state in-situ DRIFTS experiments on pure anatase-TiO_2 support. Transition-state in-situ DRIFTS experiments are conducted by alternatively switching the adsorption gas three times to first 5%CO_2 in N_2, then 20% H_2 in N_2, and finally 5% CO_2 in N_2 again under the temperature at 300 °C

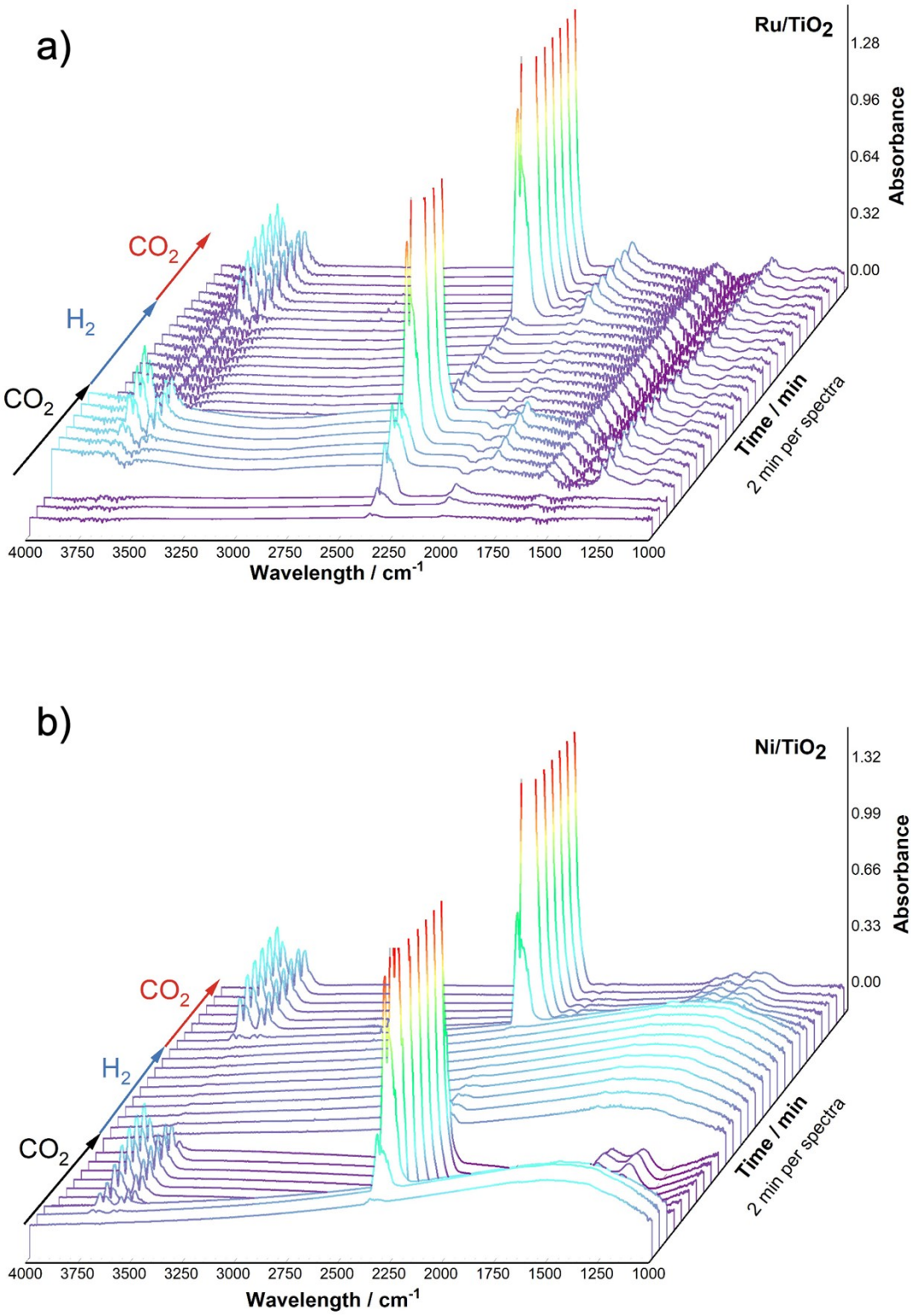

Figure. S24 3D graphs of the absorption intensity in transition-state in-situ DRIFTS experiments on (a) Ru/TiO_2 and (b) Ni/TiO_2. Transition-state in-situ DRIFTS experiments are conducted by

alternatively switching the adsorption gas three times to first 5%CO_2 in N_2, then 20% H_2 in N_2, and finally 5% CO_2 in N_2 again under the temperature at 300 °C

Table S1. The Ni (111) 2 θ angle, corresponding interplanar distance $d_{(111)}$, and lattice parameter ***a*** determined by XRD characterization

Sample	**2θ**	**d $_{(111)}$ -spacing**	***a****
NiRu/TiO_2-300	44.59	2.032	3.520
NiRu/TiO_2-500	44.48	2.036	3.522
Ni@Ru/TiO_2-300	44.56	2.033	3.521
Ni@Ru/TiO_2-500	44.48	2.036	3.522
Ru@Ni/TiO_2-300	44.53	2.035	3.521
Ru@Ni/TiO_2-500	44.48	2.036	3.522
Ni (JCPDS 004-0850)	44.78	2.02	3.494

* As Ni and the Ni-Ru solid solution in our study have face-centred cubic crystalline structures [1], the lattice parameter ***a*** and interplanar distance d_{hkl} for the (hkl) planes meet the following relationship[2]:

$$d = \frac{a}{\sqrt{h^2 + k^2 + l^2}}$$

Where, d is the lattice distance, a is the lattice constant, hkl is the Miller index.

Table. S2 Infrared band assignments of the surface species for CO_2 adsorption and hydrogenation.

Surface species	**Frequency (cm^{-1})**						Ref.
	CO_2 hydrogenation	CO_2 adsorption on Ru@Ni/TiO_2 -300	CO_2 adsorption on Ru@Ni/TiO_2 -500	CO_2 adsorption on Ru/TiO_2	CO_2 adsorption on Ni/TiO_2	CO_2 adsorption on TiO_2	
monodentate carbonate (*CO_3)	1439, 1366	1485, 1370	1357	1349	1430, 1372	1366	[3]
bicarbonate (*HCO_3)	1620	1617, 1334	1606	1615, 1328	1615, 1357	1615	[4, 5]
formate (*COOH)	1550, 1437, 2961, 2876	-	1527, 1437	1585, 1481	1516	1530, 1432	[6]
linear *CO (hc)	2020-2010	1986, 2000-2024	2015	1986, 2003-2022	-	-	[7]
bridge *CO	-	1864	-	1886	-	-	[6]
geminal *CO (lc)	2070	2070		2075	-	-	[8]
CH_4 (g)	3017, 1300	3017, 1300	-	3017, 1300	3017, 1300	3017, 1300	[9]
CO (g)	2174, 2117	2174, 2117	2147, 2117	2147, 2117	2147, 2117	2147, 2117	[10]

Table S3. Ni^0 proportion calculation results of catalysts[a].

Catalysts	Ni species	Peak area	$P(Ni^0)$[b]
$NiRu/TiO_2$-500	Ni^0	2270.93	20.5%
	NiO	857.46	
	$Ni(OH)_2$	7471.46	
Ni@Ru/TiO_2-500	Ni^0	6294.94	27.9%
	NiO	1006.73	
	$Ni(OH)_2$	15195.08	
Ru@Ni/TiO_2-500	Ni^0	3700.49	23.5%
	NiO	1180.61	
	$Ni(OH)_2$	10858.92	

a Determined from XPS measurements.

b Proportion of Ni0=Area(Ni0)/[Area(Ni0)+ Area(NiO)+ Area(Ni(OH)2)] × 100%[11].

Table S4. Surface metal concentration ratios determined by XPS results[12, 13].

Sample	**Ru/Ti ratio***	**Ru/Ni ratio***	**Ni/Ti ratio***
NiRu/TiO_2	0.019	0.776	0.024
Ni@Ru/TiO_2	0.035	0.689	0.051
Ru@Ni/TiO_2	0.018	0.178	0.101

* For two elements i, j in the sample, the concentration of i and j can be calculated by the following equation:

$$\frac{n_i}{n_j} = \frac{I_i / S_i}{I_j / S_j}$$

Where, n_i /n_j is the surface concentration precent of elements i and j; I_i and I_j are the corresponding peak intensity (peak area here) of elements i and j; S_i and S_j are the corresponding sensitivity index of elements i and j in the XPS handbook ($S_{Ni,2p\ (peak\ area)}$= 4.044, $S_{Ru,2p\ (peak\ area)}$= 4.273).

References

[1] O.U. Valdés-Martínez, C.E. Santolalla-Vargas, V. Santes, J.A. de los Reyes, B. Pawelec, J.L.G. Fierro, Influence of calcination on metallic dispersion and support interactions for NiRu/TiO2 catalyst in the hydrodeoxygenation of phenol, Catalysis Today, 329 (2019) 149-155.

[2] B.D. Cullity, Elements of X-ray Diffraction, Addison-Wesley Publishing1956.

[3] A. Cárdenas-Arenas, A. Quindimil, A. Davó-Quiñonero, E. Bailón-García, D. Lozano-Castelló, U. De-La-Torre, B. Pereda-Ayo, J.A. González-Marcos, J.R. González-Velasco, A. Bueno-López, Isotopic and in situ DRIFTS study of the CO2 methanation mechanism using Ni/CeO2 and Ni/Al2O3 catalysts, Applied Catalysis B: Environmental, 265 (2020) 118538.

[4] L. Proaño, E. Tello, M.A. Arellano-Trevino, S. Wang, R.J. Farrauto, M. Cobo, In-situ DRIFTS study of two-step CO2 capture and catalytic methanation over Ru,"Na2O"/Al2O3 Dual Functional Material, Applied Surface Science, 479 (2019) 25-30.

[5] F. Wang, S. He, H. Chen, B. Wang, L. Zheng, M. Wei, D.G. Evans, X. Duan, Active Site Dependent Reaction Mechanism over Ru/CeO2 Catalyst toward CO2 Methanation, Journal of the American Chemical Society, 138 (2016) 6298-6305.

[6] X. Xu, L. Liu, Y. Tong, X. Fang, J. Xu, D.-e. Jiang, X. Wang, Facile Cr3+-Doping Strategy Dramatically Promoting Ru/CeO2 for Low-Temperature CO2 Methanation: Unraveling the Roles of Surface Oxygen Vacancies and Hydroxyl Groups, ACS Catalysis, 11 (2021) 5762-5775.

[7] S. Chen, A.M. Abdel-Mageed, M. Dyballa, M. Parlinska-Wojtan, J. Bansmann, S. Pollastri, L. Olivi, G. Aquilanti, R.J. Behm, Raising the COx Methanation Activity of a Ru/γ-Al2O3 Catalyst by Activated Modification of Metal–Support Interactions, Angewandte Chemie International Edition, 59 (2020) 22763-22770.

[8] J.C. Matsubu, V.N. Yang, P. Christopher, Isolated Metal Active Site Concentration and Stability Control Catalytic CO2 Reduction Selectivity, Journal of the American Chemical Society, 137 (2015) 3076-3084.

[9] J. Zhou, Z. Gao, G. Xiang, T. Zhai, Z. Liu, W. Zhao, X. Liang, L. Wang, Interfacial compatibility critically controls Ru/TiO2 metal-support interaction modes in CO2 hydrogenation, Nature Communications, 13 (2022) 327.

[10] X. Li, J. Lin, L. Li, Y. Huang, X. Pan, S.E. Collins, Y. Ren, Y. Su, L. Kang, X. Liu, Y. Zhou, H. Wang, A. Wang, B. Qiao, X. Wang, T. Zhang, Controlling CO2 Hydrogenation Selectivity by Metal-Supported Electron Transfer, Angewandte Chemie International Edition, 59 (2020) 19983-19989.

[11] S. Zou, M. Zhang, S. Mo, H. Cheng, M. Fu, P. Chen, L. Chen, W. Shi, D. Ye, Catalytic Performance of Toluene Combustion over Pt Nanoparticles Supported on Pore-Modified Macro-Meso-Microporous Zeolite Foam, Nanomaterials, 2020.

[12] J. Zhou, L. Guo, X. Guo, J. Mao, S. Zhang, Selective hydrogenolysis of glycerol to propanediols on supported Cu-containing bimetallic catalysts, Green Chemistry, 12 (2010) 1835-1843.

[13] P. Yan, E. Kennedy, M. Stockenhuber, Hydrodeoxygenation of guaiacol over BEA supported bimetallic Ni-Fe catalysts with varied impregnation sequence, Journal of Catalysis, 404 (2021) 1-11.